RSC Advances

ROYAL SOCIETY OF CHEMISTRY

www.rsc.org/advances

Journal Name

ARTICLE

Sol-Gel Synthesis, Structural, Optical and Magnetic Characterization of $Ag_{3(2+x)}Pr_xNb_{4-x}O_{11+\delta}$ ($0.0 \le x \le 1.0$) Nanoparticles

Received 00th January 20xx,
Accepted 00th January 20xx

DOI: 10.1039/x0xx00000x

www.rsc.org/

S. Ramesh, [*a, d] Jerald V. Ramaclus, [b] Edgar Mosquera, [a] and B B Das [c]

In this work we have studied the optical and magnetic properties of sol–gel synthesized nanocrystalline $Ag_{3(2+x)}Pr_xNb_{4-x}O_{11+\delta}$ (x = 0.0, 0.50 and 1.0; S1-S3) samples. The structural, morphological, optical and magnetic properties of the nanoparticle were investigated using X-ray diffraction, scanning electron microscopy with energy-dispersive X-ray profile, optical absorbance spectroscopy, vibrating sample magnetometer and electron paramagnetic resonance spectroscopy. The X-ray diffraction results reveals the formation of single-phase monoclinic lattice structure with P2/m in all the samples. The optical absorption spectra indicates charge transfer from O^{2-} to Nb^{5+} of nobium and $^3H_4$ to $^1D_2$, $^3P_0$, $^3P_1$ and $^3P_2$ of preseodymium ($4f^2$) ions. Magnetic studies reveal that the samples exhibit ferromagnetism at room temperature. EPR lineshapes of the nanoparticles S1-S3 at 77 and 300 K show a broad unresolved isotropic lineshapes due to the relaxation process.

Introduction

Multifunctional materials which integrate multiple properties in a distinct material are highly desired to further the progress of research areas such as device miniaturization and in applications like high density optical and magnetic data storage system.[1-3] One such type is multiferroic materials, the promising materials for spintronic devices which display both ferromagnetic and ferroelectric properties.[4-7] However, it is a less common phenomenon due to the fact that ferromagnetic materials essentially have metals with unpaired electrons and unfilled orbitals and on the contrary ferroelectric polarization requires metals with filled orbitals.[8] Therefore it is challenging to investigate and design new multiferroic composites to combine such properties. This is demonstrated by integrating rare-earth ions as magnetic impurities into ferroelectrics. The interesting magnetic and optical properties of rare-earth ions are arisen from high-energetic intra-configurational transitions within 4fn electronic configuration and inter-configurational 4*f* and 5*d* transitions.[9] Among all rare earth ions, praseodymium (Pr^{3+}) ($4f^2$) ion has rich spectral lines in the ultra violet spectral region, and near-infrared regions owing to its elaborate energy level scheme with energy gaps of different magnitudes.[10, 11]

Silver-niobium composite is chosen as the host system due to its promising applications in ferroelectrics[12, 13] and photocatalsis.[14-17] The most vital reason is that the unique filled electronic configuration of Ag^+ ions may share in hybridization of the energy band structure.[14] Recently, several series of compounds with the general formula $Me_x(V, Nb, Ta)_{3n+1}O_{8n+3}$ (Me = Ca, Na, K, Cu, Ag) are obtained. In the above series $Ag_2Nb_4O_{11}$ is reported as stable photocatalysts, ferroelectrics and phase transitions.[18-23] The incorporation of rare-earth ion into silver-niobium system are studies on magnetic and optical property are still limited due to the problems of obtaining the homogeneous compound. Several wet and solid-state techniques have been used to synthesize the magnetic nanoparticles, such as co-precipitation,[24] hydrothermal,[25] electrochemical deposition,[26] auto combustion,[27] sol-gel,[28, 29] ball milling,[30] and vapor deposition,[31] to name a few. As each of them has different disadvantages ranging from low yield, impurity formation, extensive agglomeration to complicated synthesis schemes and investigation of alternative processing routes is still a major area which needs attention.[32, 33] Among all other methods, sol-gel technology has several advantages over the other techniques due to the stoichiometric control, ease of introducing dopants, homogeneity, and purity. Citrate nitrate gel route is promising to synthesize many novel metal oxide nanoparticle in a cost-effective manner.[33] The tri-dentate ligand behavior of the citrate ions forms a three-dimensional (3D) network in citrate nitrate gel route and decomposition of the gel leads to homogeneous mixed oxides.[34]

Therefore, in this article we present synthesis of new series of multifunctional $Ag_{3(2+x)}Pr_xNb_{4-x}O_{11+\delta}$ (x = 0.0, 0.50 and 1.0)

[a] *Laboratorio de Materiales Funcionales a Nanoescala, Departamento de Ciencia de los Materiales, Universidad de Chile, Av. Tupper 2069, Santiago, Chile.*
[b] *Department of Physics, Loyola College, Chennai 600034, India.*
[c] *Department of Chemistry, School of Physical, Chemical and Applied Sciences, Pondicherry University, Pondicherry 605014, India.*
[d] *Department of Chemistry, Saveetha School of engineering, Saveetha University, Chennai, 602105, India*

nanoparticles and exploration of their optical, magnetic and ferroelectric properties.

Experimental

Synthesis of $Ag_{3(2+x)}Pr_xNb_{4-x}O_{11+\delta}$ ($0.0 \le x \le 1.0$) nanoparticles.

Nanocrystalline $Ag_{3(2+x)}Pr_xNb_{4-x}O_{11+\delta}$ (x = 0.0, 0.50 and 1.0) are synthesized by sol-gel technique. All reagent grade chemicals are used as received without further purification. The calculated amount of precursors used to prepare $Ag_{3(2+x)}Pr_xNb_{4-x}O_{11+\delta}$ (x = 0.0, 0.50 and 1.0; S1-S3) nanoparticles are given in supplementary Table S1. The niobium citrate is prepared using the stoichiometric amount of niobium pendoxide (Nb_2O_5) mixed with hydrofluoric acid (HF) under the warm condition to get niobium fluoride complex (i.e. NbF_5^{2-}). Further, hydrated niobium pendoxide ($Nb_2O_5.nH_2O$) is precipitated by washing excess of aqueous ammonia from NbF_5^{2-}. Now, the $Nb_2O_5.nH_2O$ is dissolved in citric acid to obtain niobium citrate. The praseodymium nitrate ($Pr(NO_3)_3.nH_2O$) solution is prepared by adding nitric acid with praseodymium oxide (Pr_6O_{11}. The niobium citrate, praseodymium nitrate and silver nitrate $Ag(NO_3)$ solutions are mixed by continuous stirring for 1h at pH ~ 2-3. 30 ml of 1.5 M citric acid solution is added to this solution mixture. The resulting mixture is stirred at 333 K until it becomes a transparent gel. At that point, the gel is dried using an air oven at 473 K for 1 h. This leads to the formation of lightweight porous material due to the enormous amount of gas evolution. Finally, it is sintered at 1123 K for 4 h to obtain a fine homogeneous dense powder. The schematic synthesis of $Ag_{3(2+x)}Pr_xNb_{4-x}O_{11+\delta}$ (x = 0.0, 0.50 and 1.0; S1-S3) nanoparticles is flow charted in supplementary Figure. S1.

Characterization

The powder X-ray diffraction (XRD) data of the samples were collected by X'Pert (PANalytical) diffractometer. Monochromatic Cu Kα radiation used as a source with 40 kV/30 mA power. A scanning electron microscope (SEM, Hitchi-S3400 instrument) was used to observe the surface morphology of synthesized powders. SUPER DRYER II instrument was used to show the distribution of elements and the chemical compositions by EDX profile. The liquid displacement technique was used to determine the density of the samples. The optical absorption spectra were recorded using a Varian Cary 5000 UV-VIS-NIR spectrometer. Magnetic properties of the samples were studied by measuring magnetic moments using a LAKESHORE VSM 7404 vibrating sample magnetometer (VSM). The electron paramagnetic resonance (EPR) experiments at 77 and 300K were performed with a JEOL JES-TE 100 ESR spectrometer at 100 kHz field modulation and a phase sensitive detector to obtain first derivative signal. Quartz tubes used for recording the EPR spectra of the compounds. The magnetic field was calibrated using a Varian NMR Gauss meter and frequency meter. The magnetic field calibration was made with respect to the resonance line of DPPH (g_{DPPH} = 2.00354) as a field marker.

Results and Discussion

X-Ray Diffraction studies

Figure 1 shows powder X-ray diffraction patterns of $Ag_{3(2+x)}Pr_xNb_{4-x}O_{11+\delta}$ (x = 0.0, 0.50 and 1.0; S1-S3) nanoparticles along with corresponding (*hkl*) planes. In the XRD patterns, all the predominant peaks provide the information that the samples S1-S3 are formed in single-phase polycrystalline nature. The concentration change (x = 0.0, 0.50 and 1.0; S1-S3) does not produce any structural and phase change, but only small variations were observed in the lattice parameters. The structural information was obtained by FullProf package.[35] The diffraction patterns were indexed with the least-squares procedure to minimize the difference between the calculated and observed patterns. The refined result reveals a similar lattice parameters of monoclinic lattice sphere packing crystal structure with P2/m space group for S1-S3 samples. Lattice parameters and the unit cell volumes are gradually increasing from S1-S3 with increasing content of Pr ions (Table. 1). The crystallite sizes of the samples were calculated from the full width at half maximum (FWHM) of all the peaks using the Debye-Scherrer[36] and Williamson-Hall[37] formula. The formulae are shown in (1) and (2) respectively.

$$D = 0.89\lambda/\beta_1/2\cos\theta_{hkl} \quad \ldots. (1)$$

$$\beta\cos\theta = K\lambda/D + 2\varepsilon\sin\theta \quad \ldots. (2)$$

Where D- crystallite size, K= Scherrer constant, λ represents the wavelength of Cu Kα radiation, β stands for the corrected half width of the diffraction peak, θ is the Bragg angle of the X-ray diffraction peak and ε is the lattice strain. The samples exhibit noticeable diffraction broadening which is due to the

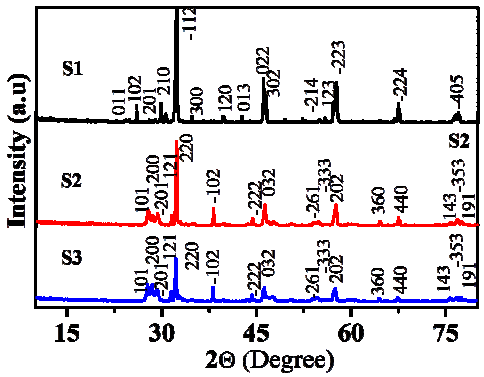

Fig. 1 Powder X-ray Diffraction patterns of $Ag_{3(2+x)}Pr_xNb_{4-x}O_{11+\delta}$ ($0.0 \le x \le 1.0$; S1-S3) nanoparticles.

increase in crystallite size from 17 to 26 nm (Table 1).[38] It is also observed that the crystallite sizes are increasing with respect to the increasing content of the Pr^{3+} ion. The increase in the crystallite size is strongly associated with the change in higher ionic radius of Pr^{3+} (1.82 Å) ions with the smaller Nb^{4+} (1.46 Å) ions. This increases the bond length in the crystal structure.[39] Density of the samples is calculated from XRD data

Table. 1 Crystal system, Lattice parameters, space group crystallite sizes and density of $Ag_{3(2+x)}Pr_xNb_{4-x}O_{11+\delta}$ (0.0, 0.25 and 1.0) (S1-S3) nanoparticles.

Sample code		S1	S2	S3
Lattice type		Mono	Mono	Mono
a (Å)		7.844	6.585	6.586
b (Å)		4.731	12.002	12.059
c (Å)		7.190	4.727	4.724
β		98.577	107.98	108.03
Unit cell volume		263.88	355.40	356.80
Z		1	1	1
Space group		P2/m	P2/m	P2/m
Crystallite Size (nm)	Scherer	17.1	19.2	26.5
	WH Plot	19.9	21.3	25.2
Density (g/cm^3)		1.99	2.88	2.06

Mono=Monoclinic

and liquid displacement method. The density of the samples does not show regular order with compositional ratio. (Table 1).

Morphology analysis

Morphological investigations were performed using SEM, and the quantitative analysis by EDX profile. The SEM micrographs of all the samples clearly reveal the regular spherical solid nanostructural particle **(Fig. 2).** The samples are found to be pores and are distributed evenly as observed from SEM images.

The randomly selected area SEM images of samples S1, S3 and S5 are shown in **Figure 2**. EDX analysis of randomly selected particle in the sample S3 conforms purity and presence of all the constituent elements. The corresponding energy profile and quantitative results of the samples S3 is shown in the **Figure 2**. X-ray mapping of the sample S3 suggest that all the constituent elements are present with uniform distribution to the entire sample and also reveals the high homogeneity and purity of the samples (**Fig. 2).**

Diffuse reflectance spectroscopy (DRS) studies

Figure 3 illustrates UV-visible diffuse reflectance spectroscopy (DRS) spectrum along with the corresponding transitions of sample S1-S3. The absorption bands appear at 272, 387, 450, 473, 486, and 590 nm. The strong absorbance at 272 and 387 nm attributed to inter-band charge transfer from O^{2-} 2p electron states to Nb^{5+} 4d electron states. The *4f-4f* transitions have been studied extensively for Pr^{3+} ions[40-42] and the information on the *4f-5d* absorption is still limited.[43, 44] Sugar[45] and Cross white, Dieke and Carter[46] conducted preliminary studies on free ion and they identified the *4f-5d* bands begin over 193 nm (61000 cm^{-1}) above the $^3H_4$ ($4f^2$) ground state[47] where exists six $4f^2$ manifolds which are considerably lower energy than the *4f-5d* band. These levels give rise to the *4f-4f* fluorescence bands which is often studied in Pr^{3+} ions doped solids.[48] In the absorption spectra the sharp absorption bands

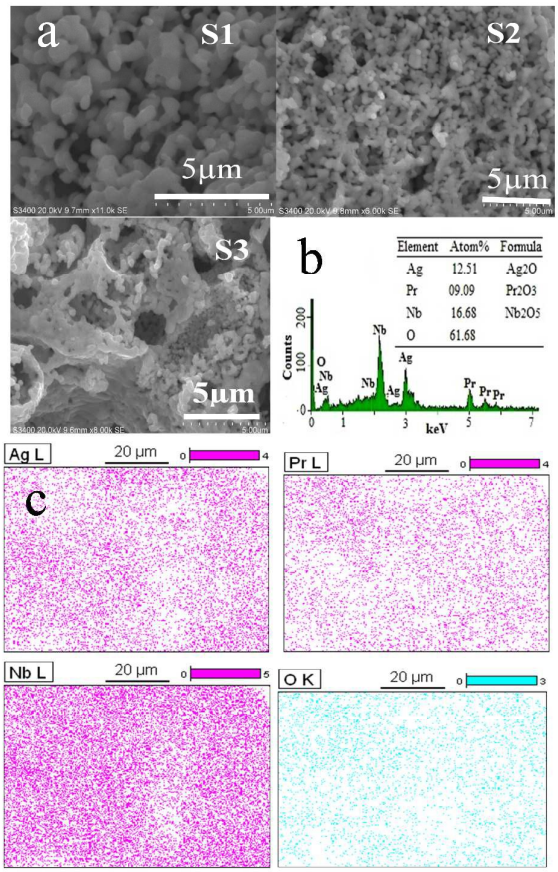

Fig. 2 (a) The SEM images of $Ag_{3(2+x)}Pr_xNb_{4-x}O_{11+\delta}$ ($0.0 \le x \le 1.0$; S1-S3) nanoparticles (b) EDX- profile of S3 and X-ray mapping of S3.

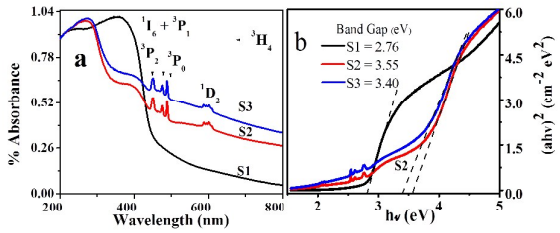

Fig. 3 (a) DRS spectra and (b) Tauc plot of $Ag_{3(2+x)}Pr_xNb_{4-x}O_{11+\delta}$ ($0.0 \le x \le 1.0$; S1-S3) nanoparticles

at 590, 486, 473 and 450 nm are due to the transitions from the ground state $^3H_4$ to the excited states $^1D_2$, $^3P_0$, $^3P_1$ and $^3P_2$ of Pr^{3+} ($4f^2$) ions.[49] These three transitions are the identified as emission of 645nm. The transition from $^3H_4$ to $^3P_0$ is specifically responsible for application in commercial blue laser diode, blue and blue-greenish LEDs.[50] The effective absorption band of the most photosensitizers (PS), as observed in the present case holds great promise for photodynamic therapy (PDT) treatment

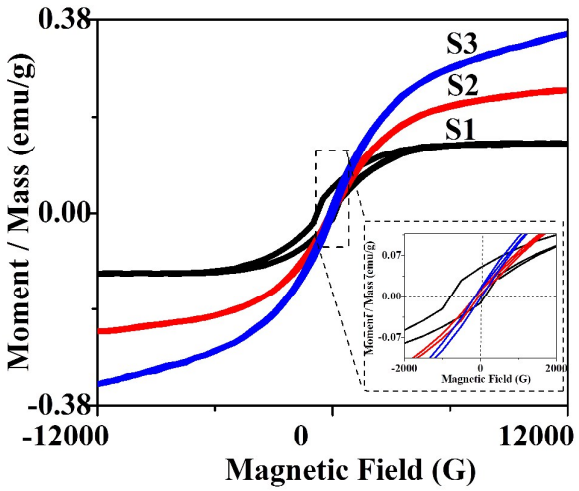

Fig. 4 Pictorial flowchart representation for the synthesis of $Ag_{3(2+x)}Pr_xNb_{4-x}O_{11+\delta}$ ($0.0 \le x \le 1.0$) (S1-S3) nanoparticle.

and clinical trials. The sharp absorption bands indicate the intrinsic band gap transition of the sample. The band gap of the semiconductor $Ag_{3(2+x)}Pr_xNb_{4-x}O_{11+\delta}$ (S1-S3) are estimated with

Tauc plot is shown in Figure 5 (a). The results indicate that the samples S1-S3 exhibit an indirect wide band gap of 2.76, 3.57, and 3.40 eV respectively. The reported indirect band gaps of $Na_2Ta_4O_{11}$, $PbTa_4O_{11}$, $Ag_2Ta_4O_{11}$ and $Ag_2Nb_4O_{11}$ are 4.3, 3.95, 3.9, 3.30 eV respectively.[23] The current studied sample $Ag_6Nb_4O_{11+\delta}$ shows a 0.05 eV narrower band gap than $Ag_2Nb_4O_{11}$ and 0.64 eV narrower than Nb_2O_5 (3.4 eV). The result suggests that the valence band (VB) electrons are easily excited to the photocatalytic activity due to Ag^+ into Niobium system.

Magnetic Studies

Vibrating Sample Magnetometer

Figure 4 illustrate the typical magnetisation curve and hysteresis of the synthesised nanoparticle. The magnetic moment versus magnetic field curve was recorded in the range of ±12000 G at 300 K. The magnetization curve of the samples S1-S3 reveals their ferromagnetic behaviour. The magnetic susceptibility, (χ) of the samples are calculated using the relation (3) bellow,

$$M = \chi H \quad \ldots (3)$$

where M -Magnetization (emu/gm) and H -Applied magnetic field. The magnetic susceptibility of the sample increases with respect to increase in Pr ions. The susceptibility value increases from 2.56 $x10^{-6}$ emu/gG for S1 (where no Pr ions are present) to 4.34 $x10^{-4}$ emu/g for S3 (where maximum Pr ions are present). The observed values of Magnetic susceptibility, (χ), Saturation magnetization (Ms), Remanence (Mr), Magnetic coercivity (Hci) and Squareness ratio (S) of $Ag_{3(2+x)}Pr_xNb_{4-x}O_{11+\delta}$ (x = 0.0, 0.50 and 1.0; S1-S3) nanonanoparticle are given in Table 2. The sample S1 shows the complete saturation magnetization at 0.004 emu/g and sample S2- S3 do not show such complete saturation even at the magnetic field of ±12000 G. The low value of Ms, 0.13 emu/g for S1, indicates the presence of nanocrystallites in the sample[51] and the crystallite size is almost near to the single domain sizes.[52] Once the Pr^{3+} ($4f^2$) ions are incorporated into the sample, the Ms values increase to maximum level of 0.35 emu/g as evidenced in S3. The incensement of the Ms is due to the incenses of crystallite sizes[53] that may refer to the surface contribution, defects, and stoichiometric deviation.[54] The perfect crystal magnetizes easily because the whole bulk is in a single domain and all the electrons are lined up at low Ms. In polycrystalline materials, there are many crystals with axis at different orientations and within each crystal some domains are present. Once the magnetic field is applied to the polycrystalline materials, the domain walls begin to move to the favourable direction of magnetization.[55] After demagnetization the magnetic spins are rearranged and reach Mr and Hci. The low values of the Hci may be due to the small crystallite size are explained with random anisotropy model.[56] The magneto crystalline anisotropy constant can be averaged over some grains with the following consequence, lesser the crystallite size lower the coercivity within the critical size but above critical size the greater the size the lesser the Hci. The Hci values decreases with the increasing crystallite size from S1-S3 and this results the nanocrystalline structure to become excellent soft magnetic materials.[57, 58]. The shape of a hysteresis loop is determined partly by the domain state. The hysteresis loops for single domains are typically wider than the multi domain materials. This is just a consideration of the higher Hci and Mr in single domain material. The squareness ratio (S) is given by the ratio of S (S = Mr/Ms) and is essentially a measure of the hysteresis loop in distinguishing the domain state. In general, large squareness ratio values are desired for hard magnetic materials which are used in data storage applications. The value of S in the range from 0.002 to 0.35 suggests that the samples are having multi domain systems.[59] The small width of the hysteresis which has low Hci and S can also contribute to decrease in energy loss during magnetization. The smooth morphology of the sample leads to the low inner residual stress which exhibit good mechanical properties. The small squareness ratio of the samples indicates that these

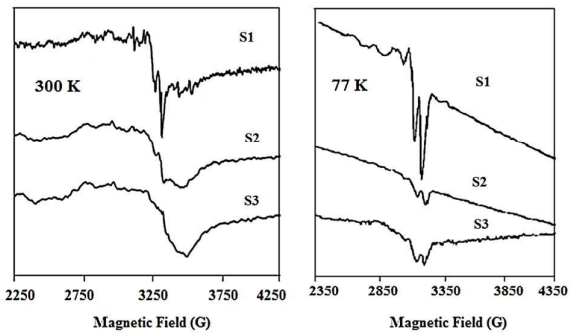

Fig. 5 Magnetization plot $Ag_{3(2+x)}Pr_xNb_{4-x}O_{11+\delta}$ ($0.0 \le x \le 1.0$; S1-S3)nanoparticles at 300 K and 77 K

nanoparticles can be promising candidates for microelectromechanical systems (MEMS).[60] The smooth hysteresis loop proves the homogeneity of the nanoparticle.

Electron Spin Resonance

To gain further insight into the nature of magnetization, we studied the EPR spectra at 300 and 77 K due the presence of the paramagnetic species (Nb and Pr) in the nanoparticles. The Nb^{4+} ion (^{93}Nb Nuclear spin I= 9/2; natural abundance: 100%) should yield hyperfine structure composed of ten lines, and for the Pr^{3+} (^{141}Pr; I= 5/2; natural abundance: 100.00 %) six lines. Figure 5 shows the EPR spectra of $Ag_{3(2+x)}Pr_xNb_{4-x}O_{11+\delta}$ (x = 0.0, 0.50 and 1.0; S1-S3) nanoparticles at 300 and 77 K. The calculated g values of $Ag_{3(2+x)}Pr_xNb_{4-x}O_{11+\delta}$ (x = 0.0, 0.50 and 1.0; S1-S3) nanoparticles are presented in Table 2. The sample S1 show a week resolved peak centred at g = 2.039 at 300 K which is likely due to the aggregates of reduced Nb^{4+} ions[61] and this in agreement with the optical absorption spectra. The presence of a poor hyperfine structure of S1 at 300 and 77 K indicates the onset of dipolar interaction between niobium ions. The hyperfine splitting of the sample S2 and S3 at 300 and 77 K were collapsed, and only a broad lineshape is observed after the addition of Pr^{3+} ions into the samples. This broadening of the lineshapes increases with respect to pr^{3+} ionic concentration. In addition to the incorporation of rare earth ions (Pr^{3+} ions) into the transition metal compounds, the crystalline structure is crucial to explain EPR.[62] The Pr^{3+} ($4f^2$) are non-Kramer's ions, but it has a magnetic moment. The hyperfine lineshapes were not observed even at 77 K due to the rapid electronic conduction of Nb_2O_5. The room-temperature EPR spectra of the samples show the resonance at g = 2.30 this is an indication of the presence of distorted NbO_6 structural units in the semiconductor network.[63] At higher concentrations of pr^{3+} ions, the intensity of the EPR signals decreases. The reduction of the EPR signals are due to various reasons, such as paramagnetic ions coupled by strong exchange interactions,[64] spin-spin interaction between neighbouring paramagnetic ions of different elements and a process involving redox phenomena.[65] The reduction of the signal in the present study at higher concentrations of Pr^{3+} ($4f^2$) may be due to relaxation process involving interactions between Nb^{4+} ions and praseodymium ions.

Conclusions

Novel $Ag_{3(2+x)}Pr_xNb_{4-x}O_{11+\delta}$ (x = 0.0, 0.50 and 1.0; S1-S3) nanoparticles of monoclinic lattice type with P2/m space group were successfully synthesized by sol gel technique. The morphology of the samples shows spherical in shape, and all the constituent elements are distributed homogenously. The absorption spectra show the indirect band gap for the samples which can be useful for photocatalytic application and the absorption of $^3H_4$ to $^3P_0$ may be used for the blue laser diode, blue and blue-greenish LEDs. The low value of the remanence and coercivity reveals that the samples are in the category of the soft magnetic materials. The presence of a poor EPR hyperfine structure indicates the onset of dipolar interaction between niobium ions.

Table.2. Observed values of Magnetic susceptibility, (χ), saturation magnetization (Ms), remanence (Mr), magnetic coercivity (Hci) and squareness ratio (S) Spin-Hamiltonian parameters of $Ag_{3(2+x)}Pr_xNb_{4-x}O_{11+\delta}$ (0.0 ≤ x ≤ 1.0) (S1-S3) nanoparticles.

Code		S1	S2	S3
Hci (G)		108.60	88.17	87.05
Mr (emu/g) x10^{-3}		11.99	6.89	8.84
Ms (emu/g)		0.13	0.24	0.35
S= (Mr/Ms)		0.043	0.028	0.025
χ (emu/gG)		2.7x10^{-5}	3.9x10^{-5}	5.2x10^{-5}
k		788.35	356.92	241.89
g matrix	300 K	2.0391	2.0320	2.0219
	77K	2.0542	2.0512	2.0518

Acknowledgements

The authors (RS and EM) are thankful to the CONICYT-PIA (Grant no. ACT 1117).

Notes and references

Corresponding Author E-mail: rameshsiva_chem@yahoo.com

† Electronic Supplementary Information (ESI) available: Figure SF1. Flow chart of the synthesis and Table. ST1. Calculated amount precursors of $Ag_{3(2+x)}Pr_xNb_{4-x}O_{11+\delta}$ (0.0 ≤ x ≤ 1.0) (S1-S3) nanoparticles.

References

1. L. Nicole, C. Laberty-Robert, L. Rozes and C. Sanchez, *Nanoscale*, 2014, **6**, 6267-6292.
2. A. Rehman and X. Zeng, *RSC Advances*, 2015, **5**, 58371-58392.
3. A. Tyagi, K. M. Tripathi and R. K. Gupta, *Journal of Materials Chemistry A*, 2015, DOI: 10.1039/c5ta05666g.
4. M. K. Gupta, R. Mittal, M. Zbiri, N. Sharma, S. Rols, H. Schober and S. L. Chaplot, *Journal of Materials Chemistry C*, 2015, DOI: 10.1039/c5tc02096d.
5. X. Z. Zhai, H. M. Deng, W. L. Zhou, P. X. Yang, J. H. Chu and Z. Zheng, *RSC Advances*, 2015, **5**, 82351-82356.
6. D. Sando, A. Agbelele, D. Rahmedov, J. Liu, P. Rovillain, C. Toulouse, I. C. Infante, A. P. Pyatakov, S. Fusil, E. Jacquet, C. Carrétéro, C. Deranlot, S. Lisenkov, D. Wang, J. M. Le Breton, M. Cazayous, A. Sacuto, J. Juraszek, A. K. Zvezdin, L. Bellaiche, B. Dkhil, A. Barthélémy and M. Bibes, *Nat Mater*, 2013, **12**, 641-646.
7. R. Koferstein and S. G. Ebbinghaus, *RSC Advances*, 2015, **5**, 71491-71499.
8. P. Jarupoom, S. Eitssayeam, K. Pengpat, T. Tunkasiri, D. Cann and G. Rujijanagul, *Nanoscale Research Letters*, 2012, **7**, 59.

9. S. Ramesh and B. B. Das, *Journal of the Korean Chemical Society*, 2011, **55**, 502-508.
10. E. Sarantopoulou, Z. Kollia, A. C. Cefalas, V. V. Semashko, R. Yu. Abdulsabirov, A. K. Naumov, S. L. Korableva, T. Szczurek, S. Kobe and P. J. McGuiness, *Optics Communications*, 2002, **208**, 345-358.
11. D. I. Woodward and R. Beanland, *Inorganic Chemistry*, 2014, **53**, 8941-8948.
12. M. Yashima, S. Matsuyama, R. Sano, M. Itoh, K. Tsuda and D. Fu, *Chemistry of Materials*, 2011, **23**, 1643-1645.
13. F. Desheng, E. Makoto, T. Hiroki, T. Tomoyasu, I. Mitsuru and K. Shin-ya, *Journal of Physics: Condensed Matter*, 2011, **23**, 075901.
14. H. Dong, G. Chen, J. Sun, Y. Feng, C. Li and C. Lv, *Chemical Communications*, 2014, **50**, 6596-6599.
15. L. Yang, J. Liu, H. Chang and S. Tang, *RSC Advances*, 2015, **5**, 59970-59975.
16. G. Li, S. Yan, Z. Wang, X. Wang, Z. Li, J. Ye and Z. Zou, *Dalton Transactions*, 2009, DOI: 10.1039/b906799j, 8519-8524.
17. D. Xu, S. Yang, Y. Jin, M. Chen, W. Fan, B. Luo and W. Shi, *Langmuir*, 2015, **31**, 9694-9699.
18. S. Zhang, W. Li, C. Li and J. Chen, *The Journal of Physical Chemistry B*, 2006, **110**, 24855-24863.
19. Y. Liang, L. F. Zhu, P. Liu, H. B. Li, J. Xiao, X. W. Ji and G. W. Yang, *Crystengcomm*, 2013, **15**, 6131-6135.
20. N. Maso, D. I. Woodward, P. A. Thomas, A. Varez and A. R. West, *Journal of Materials Chemistry*, 2011, **21**, 2715-2722.
21. N. Maso and A. R. West, *Journal of Solid State Chemistry*, 2015, **225**, 438-449.
22. H. Dong, G. Chen, J. Sun, C. Li, C. Lv and Y. Hu, *Physical Chemistry Chemical Physics*, 2015, **17**, 795-799.
23. J. Boltersdorf, T. Wong and P. A. Maggard, *Acs Catalysis*, 2013, **3**, 2943-2953.
24. A.B. Gadkaria, , T.J. Shindeb, P.N. Vasambekarc *Materials Chemistry and Physics*, 2009, **114**, 505–510.
25. X. Zhang, Q. Wang, J. Zhang, J. Wang, M. Guo, S. Chen, C. Li, C. Hu and Y. Xie, *RSC Advances*, 2015, **5**, 89976-89984.
26. G.-R. Li, D.-L. Qu, L. Arurault and Y.-X. Tong, *The Journal of Physical Chemistry C*, 2009, **113**, 1235-1241.
27. F. Gu, S. F. Wang, M. K. Lü, G. J. Zhou, D. Xu and D. R. Yuan, *Langmuir*, 2004, **20**, 3528-3531.
28. G. D. Dwivedi, M. Kumar, P. Shahi, A. Barman, S. Chatterjee and A. K. Ghosh, *RSC Advances*, 2015, **5**, 30748-30757.
29. F. Cheng, C. Liao, J. Kuang, Z. Xu, C. Yan, L. Chen, H. Zhao and Z. Liu, *Journal of Applied Physics*, 1999, **85**, 2782-2786.
30. H. K. Yang and J. H. Jeong, *The Journal of Physical Chemistry C*, 2010, **114**, 226-230.
31. T. M. Al Tahtamouni, X. Du, J. Lin and H. Jiang, *Opt. Mater. Express*, 2015, **5**, 648-654.
32. J. Lin and Q. Su, *Journal of Materials Chemistry*, 1995, **5**, 603-606.
33. L. Schmidt, A. Dimitrov and E. Kemnitz, *Chemical Communications*, 2014, **50**, 6613-6616.
34. A. Sutka and G. Mezinskis, *Front. Mater. Sci.*, 2012, **6**, 128-141.
35. J. Rodríguez-Carvajal, *Physica B: Condensed Matter*, 1993, **192**, 55-69.
36. S. Ramesh, *Journal of Nanoscience*, 2013, **2013**, 1-8.
37. G. K. Williamson and W. H. Hall, *Acta Metallurgica*, 1953, **1**, 22-31.
38. B. G. Kumar and K. Muralidharan, *RSC Advances*, 2014, **4**, 28219-28224.
39. C. Rath, S. Anand, R. P. Das, K. K. Sahu, S. D. Kulkarni, S. K. Date and N. C. Mishra, *Journal of Applied Physics*, 2002, **91**, 2211-2215.
40. K. Krambrock, K. J. Guedes, S. Schweizer, J. M. Spaeth and J. Y. Gesland, *Journal of Alloys and Compounds*, 2002, **344**, 246-250.
41. M. A. Gagnani, R. S. Shukla and S. N. Misra, *Spectrochimica Acta Part A: Molecular and Biomolecular Spectroscopy*, 2005, **61**, 535-539.
42. G. Blasse, A. Meijerink and C. de Mello Donegá, *Journal of Alloys and Compounds*, 1995, **225**, 24-27.
43. P. A. Tanner, C. S. K. Mak and M. D. Faucher, *Chemical Physics Letters*, 2001, **343**, 309-314.
44. C.-K. Duan and S. Jiang, *Spectroscopy Letters*, 2010, **43**, 423-430.
45. J. Sugar, *J. Opt. Soc. Am.*, 1965, **55**, 1058-1059.
46. H. M. Crosswhite, G. H. Dieke and W. J. Carter, *The Journal of Chemical Physics*, 1965, **43**, 2047-2054.
47. Z. Cai, V. M. Umar and C. Froese Fischer, *Physical Review Letters*, 1992, **68**, 297-300.
48. J. Ganem, W. M. Dennis and W. M. Yen, *Journal of Luminescence*, 1992, **54**, 79-87.
49. T. Som and B. Karmakar, *Spectrochimica Acta Part A: Molecular and Biomolecular Spectroscopy*, 2011, **79**, 1766-1782.
50. J. Yang, B. J. Chen, E. Y. B. Pun, B. Zhai and H. Lin, *Opt. Express*, 2013, **21**, 1030-1040.
51. H. Z. Shouheng Sun , David B. Robinson , Simone Raoux , Philip M. Rice , Shan X. Wang , and Guanxiong Li *Journal of the American Chemical Society*, 2004, **126**, 7.
52. C.-Y. Lin, K.-C. Lee and Y. D. Yao, *Solid State Communications*, 1992, **83**, 371-374.
53. R. H. Goncalves, C. A. Cardoso and E. R. Leite, *Journal of Materials Chemistry*, 2010, **20**, 1167-1172.
54. N. Feltin and M. P. Pileni, *Langmuir*, 1997, **13**, 3927-3933.
55. R. Wieser, E. Y. Vedmedenko and R. Wiesendanger, *Physical Review Letters*, 2011, **106**, 067204.
56. G. Herzer, *Journal of Magnetism and Magnetic Materials*, 1996, **157–158**, 133-136.
57. R. Skomski, *Journal of Physics: Condensed Matter*, 2003, **15**, R841.
58. R. Hamzaoui, O. Elkedim and E. Gaffet, *Materials Science and Engineering: A*, 2004, **381**, 363-371.
59. C.-W. Chen, in *Magnetism and Metallurgy of Soft Magnetic Materials*, ed. C.-W. Chen, Elsevier, 1977, DOI: http://dx.doi.org/10.1016/B978-0-7204-0706-8.50010-1, pp. 61-97.
60. L. Zhongliang, S. Xuming, Z. Yang and Z. Haixia, *Journal of Micromechanics and Microengineering*, 2013, **23**, 085013.
61. F. Dolci, M. Chio, M. Baricco and E. Giamello, *J Mater Sci*, 2007, **42**, 7180-7185.

62. B. B. Das and S. Ramesh, *AIP Conference Proceedings*, 2008, **1003**, 85-87.
63. P. F. Chester, *Journal of Applied Physics*, 1961, **32**, 866-868.
64. I. Ardelean, O. Cozar and G. Ilonca, *Journal of Non-Crystalline Solids*, 1984, **68**, 33-42.
65. R. Harani, C. A. Hogarth and K. A. K. Lott, *J Mater Sci*, 1984, **19**, 1420-1427.

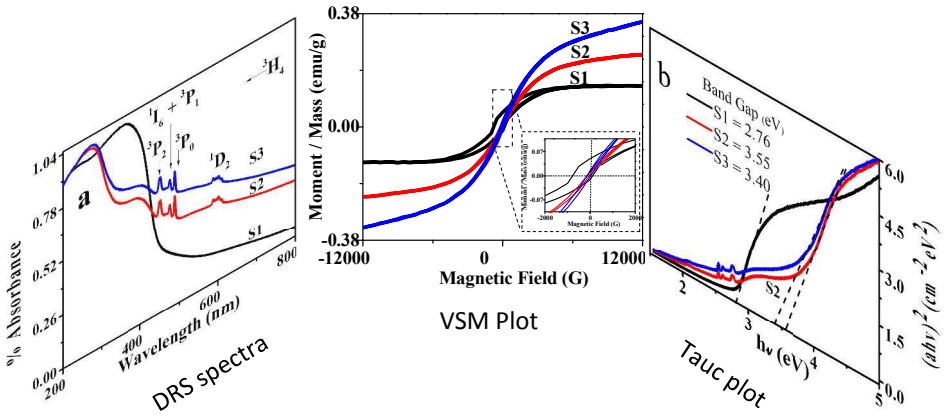

- In this work we have studied the optical and magnetic properties of sol–gel synthesized nanocrystalline $Ag_{3(2+x)}Pr_xNb_{4-x}O_{11+\delta}$ (x = 0.0, 0.50 and 1.0; S1-S3) samples.
- The structural, morphological, optical and magnetic properties of the nanoparticle were investigated using X-ray diffraction, scanning electron microscopy with energy-dispersive X-ray profile, optical absorbance spectroscopy, vibrating sample magnetometer and electron paramagnetic resonance spectroscopy.
- The X-ray diffraction results reveals the formation of single-phase monoclinic lattice structure with P2/m in all the samples.
- The optical absorption spectra indicates charge transfer from O^{2-} to Nb^{5+} of nobium and $^3H_4$ to $^1D_2$, $^3P_0$, $^3P_1$ and $^3P_2$ of preseodymium ($4f^2$) ions. Magnetic studies reveal that the samples exhibit ferromagnetism at room temperature.
- EPR lineshapes of the nanoparticles S1-S3 at 77 and 300 K show a broad unresolved isotropic lineshapes due to the relaxation process.